DIFFUSION-LIMITED REACTIONS IN NANOSCALE ELECTRONICS*

RYAN M. EVANS †, ARVIND BALIJEPALLI ‡, AND ANTHONY J. KEARSLEY §

Abstract. A partial differential equation (PDE) is developed to describe time-dependent receptor-ligand interactions for applications in biosensing with biological field-effect transistors (Bio-FETs). This model describes biochemical interactions on a biochemical gate at the sensor surface, which results in a time-dependent change in the Bio-FET's conductance. It was shown that one can exploit the disparate length scales of the solution-well and biochemical gate to reduce the coupled PDE model to a single nonlinear integrodifferential equation (IDE) that describes the concentration of reacting species. Although this equation has a convolution integral with a singular kernel, a numerical approximation is constructed by applying the method of lines. The need for specialized quadrature techniques is obviated and numerical evidence shows that this method achieves first-order accuracy. Results reveal a depletion region on the biochemical gate, which non-uniformly alters the surface potential of the semiconductor.

Key words. Biological field effect transistor, integrodifferential equation, method of lines.

Mathematics Subject Classification. 35Q92, 41A60, 65R20, 92C40.

1. Introduction. The ability to tailor therapies to individuals or specific subsets of a population to deliver personalized care has the potential to fundamentally remake healthcare delivery. The most promising therapeutic candidates for such targeted care are new classes of biologic drugs based on naturally occurring molecules, made possible due to rapid advances in genomics and proteomics [10, 26]. Importantly, such therapies can be safer and yield better outcomes at lower doses when treating debilitating conditions such as diabetes, Alzheimer's disease, or certain cancers [2, 7]. The widespread use of personalized care is currently limited by our ability to routinely measure pathology in individuals including biomarkers, metabolites, tissue histology, and gene expression. Moreover, existing clinical diagnostics are cumbersome, require specialized facilities, can take days to weeks to perform, and are in many cases prohibitively expensive. This has led to the development of new portable detection tools including antibody-based lateral flow assays [8, 19], microelectromechanical sensor (MEMS) based resonators that can detect binding of biomarkers to the sensor surface [15, 16, 21, 23], surface plasmon resonance [17, 27], ring cavity resonators [1, 4, 24], and electronic measurements with biological field-effect transistors (Bio-FETs) [6, 20, 22, 28]. The latter are particularly well-suited for biomarker measurements due their high charge sensitivity and direct signal transduction, allowing label-free measurements at physiological concentrations. Furthermore, by leveraging semi-conductor processing techniques, measurements with Bio-FETs can be made massively parallel, cost-effective, and portable.

A Bio-FET is a three-terminal device represented in Figure 1.1. A semiconductor channel between the source and drain terminals conducts a current that is strongly modulated by an electrostatic potential applied to the gate. Biomarkers in aque-

†Applied and Computational Mathematics Division, National Institute of Standards and Technology, Gaithersburg, MD 20899, USA (ryan.evans@nist.gov).

‡Engineering Physics Division, National Institute of Standards and Technology, Gaithersburg, MD 20899, USA (arvind.balijepalli@nist.gov).

§Applied and Computational Mathematics Division, National Institute of Standards and Technology, Gaithersburg, MD 20899, USA (anthony.kearsley@nist.gov).

ous solution exhibit a well-defined electrostatic surface potential [5, 14] arising from charged hydrophilic residues that interact with water. When these molecules adsorb to the Bio-FET's biochemical gate, they strongly modulate the channel current proportional to the magnitude of their surface potential. This allows Bio-FETs to be used to detect and quantify biomarkers adsorbed to the biochemical gate. Furthermore, functionalizing the Bio-FET, by attaching molecules to the gate surface that have a high inherent affinity for biomarkers of interest (see Figure 1.1), allows measurements with high specificity that are tailored to one or more biomarkers of interest.
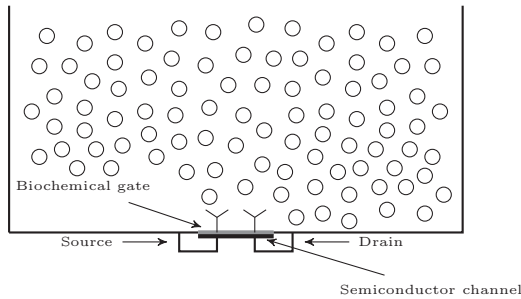

FIG. 1.1: *Schematic of biomarker measurements with a Bio-FET. Ligand molecules injected at the top of the solution-well diffuse and bind with receptors immobilized on the Bio-FET's biochemical gate. This schematic is not drawn to scale. In particular, the width of the solution-well is of on the order of millimeters, and substantially larger than the size of the biochemical gate, which spans micrometers. See Table 2.1 for exact parameter values.*

An accurate and dynamical model of receptor-ligand interactions at the biochemical gate is a critical component in maximizing the sensitivity of Bio-FET-based measurements. Specifically, quantitative descriptions of the distribution of adsorbed ligands and their surface potentials can be combined with a model of the semi-conductor physics to refine predictions of the measured signal. This in turn can be used to optimize sensor design, particularly the geometry of the biochemical gate. An accurate quantitative description of the concentration of adsorbed ligands on the biochemical gate must account for the coupling between diffusion and reaction on the biochemical gate. To the authors' knowledge this is a previously unexplored area of mathematical inquiry, though Poisson-Boltzman approaches to model sensor physics have been studied. For example in [13] Heitzinger *et al.* use the Poisson-Boltzman equation to develop a multiple-scale model for the electric potential distribution within semiconductors of planar and nanowire field-effect biosensors. Therein, the authors model these devices using three layers: a semiconductor layer, a dielectric layer, and a discrete layer of biomolecules immobilized on the dieletric layer. Homogenization techniques are employed to reconcile the biomolecule length scale with the semiconductor length scale, and interface conditions for the biomolecule-dielectric interface are derived. It must be noted that there are several important differences between [13] and the present manuscript. Perhaps the most important is that while [13] focuses on the electric potential distribution within the semiconductor channel, the present manuscript models the coupling between reaction and diffusion. Furthermore, while the authors of [13] model the biomolecule layer with a discrete number of biomolecules and use homogenization techniques, in the present manuscript a continuum perspective is presented. Finally, [13] assumes a *steady* distribution of biomolecules on the dielectric layer, while the present manuscript concerns the time-evolution of the concentration of bound ligand on the surface which is directly related to the measured

signal.

In [18] the one-dimensional Poisson-Boltzman equation was employed to model the electrostatic potential from a layer of biological macromolecules on the biochemical gate of a metal-oxide-semiconductor transistor. In contrast, [3] uses a three-dimensional model of the electric potential in semiconductor channel, and couples the aqueous and semiconductor regions through interface conditions obtained from Monte Carlo simulations, which provide an estimate of the charge distribution from adsorbed biomolecules on the biochemical gate.

In [25] Heitzinger, Mauser, and Ringhofer calculate numerical values for the kinetic parameters governing adsorption and desorption processes of CO at a SnO_2 single-nanowire gas sensor. The authors adopt a continuum perspective by modeling surface reactions on a single-nanowire gas sensor through a set of differential equations. However, in [25] the authors simply apply the well-stirred kinetics approximation in which gaseous carbon monoxide transport is completely divorced from adsorption and desorption processes at the surface. This reduces their model to a set of nonlinear ordinary differential equations (ODE), which can be used to estimate kinetic rate constants involved in the reaction of interest.

In the present manuscript a quantitative description of the coupling between reaction and diffusion in Bio-FETs is developed. In particular, we consider the experimentally relevant limit of very low ligand concentrations–*i.e.*, on the order of pico- to femtomolar–and very fast assocation rates. This problem is particularly challenging due to the disparate time and length scales involved. For example, the length scales span three orders of magnitude, ranging from order of millimeters for the solution-well to micrometers for the biochemical gate. Combining this fact with the diffusion-limited nature of the kinetics under consideration leads to the conclusion that the time-evolution of the reacting species concentration depends heavily on a diffusive boundary layer near the surface.

2. Governing Equations.

2.1. Mathematical Model. We take our domain to be the rectangle $[0, \widetilde{L}] \times [0, \widetilde{H}]$ shown in Figure 1.1, with the origin at the lower-left corner of the solution-well. The parameters $\widetilde{L}$ and $\widetilde{H}$ are the length and height of the solution-well respectively; for parameter values see Table 2.1. Throughout the manuscript tildes are used to denote dimensional quantities. Receptors are confined to the biochemical gate, which occupies the very narrow strip $[-\widetilde{l}_s/2 + \widetilde{L}/2, \ \widetilde{L}/2 + \widetilde{l}_s/2] \times 0 = [\widetilde{x}_{\min}, \widetilde{x}_{\max}] \times 0$, where $\widetilde{l}_s$ denotes the biochemical gate length and $[\widetilde{x}_{\min}, \widetilde{x}_{\max}] := [-\widetilde{l}_s/2 + \widetilde{L}/2, \ \widetilde{L}/2 + \widetilde{l}_s/2]$. It is important to note the disparate length scales involved: while the solution-well length scale is on the order of millimeters, the biochemical gate spans micrometers and is three orders of magnitude smaller.

Assuming that ligand molecules are continuously and uniformly injected at the top of the well, ligand transport is governed by the diffusion equation, expressed in dimensionless form as:

$$\frac{\partial C}{\partial t} = D_{\mathrm{w}} \left(\epsilon^2 \frac{\partial^2 C}{\partial \overline{x}^2} + \frac{\partial^2 C}{\partial \overline{y}^2} \right), \tag{2.1a}$$

$$C(\overline{x}, \overline{y}, 0) = 0, \tag{2.1b}$$

$$C(\overline{x}, 1, t) = 1, \tag{2.1c}$$

$$\frac{\partial C}{\partial \overline{x}}(0, \overline{y}, t) = \frac{\partial C}{\partial \overline{x}}(1, \overline{y}, t) = 0. \tag{2.1d}$$

TABLE 2.1: *Bounds for dimensional and dimensionless parameters are given below.*

Dimensional Parameters		Dimensionless Parameters	
Parameter	Range	Parameter	Range
$\widetilde{D}$ (cm^2/s)	10^{-6}	D_{w}	2.5×10^{-2} to 2.5×10^2
$\widetilde{k}_{\mathrm{a}}$ (cm$^3 \cdot$ (mol $\cdot$ s)$^{-1}$)	10^{11} to 10^{12}	D	4×10^3 to 4×10^7
$\widetilde{k}_{\mathrm{d}}$ (s^{-1})	10^{-5} to 1	$\mathrm{Da_w}$	1.33×10^3 to 2.66×10^3
$\widetilde{C}_{\mathrm{u}}$ (mol $\cdot$ cm^{-3})	10^{-18} to 10^{-15}	Da	3.32 to 66.42
$\widetilde{R}_{\mathrm{t}}$ (mol $\cdot$ cm^{-2})	6.6422×10^{-14} to 1.3284×10^{-13}	K	10^{-2} to 10^6
$\widetilde{H}$ (cm)	0.2	ϵ	0.4
$\widetilde{L}$ (cm)	0.5	l_{s}	10^{-3}
$\widetilde{l}_s$ (cm)	5×10^{-4}		

Equation (2.1a) governs ligand transport in the interior of our domain Ω for positive time t, (2.1b) is the initial condition, (2.1c) imposes a continuous and uniform ligand injection through the top boundary, and (2.1d) imposes no flux of ligand through the left and right boundaries. The authors studied a sealed experiment in [9] by replacing (2.1b) with a compactly supported Gaussian to model ligand injection, and the inhomogeneous Dirichlet condition (2.1c) with a homogeneous Neumann condition.

In writing (2.1a)–(2.1d), the spatial variables $\widetilde{x}$ and $\widetilde{y}$ have been nondimensionalized with the solution-well dimensions by setting $\overline{x} = \widetilde{x}/\widetilde{L}$ and $\overline{y} = \widetilde{y}/\widetilde{H}$. Since we are interested in reaction dynamics on the biochemical gate the time variable has been scaled with the forward reaction rate–*i.e.*, the product of the association rate constant $\widetilde{k}_{\mathrm{a}}$ and the total ligand concentration in the solution-well $\widetilde{C}_{\mathrm{u}}$–by setting $t = \widetilde{k}_{\mathrm{a}}\widetilde{C}_{\mathrm{u}}\widetilde{t}$. In equation (2.1a) the parameter $\epsilon = \widetilde{H}/\widetilde{L}$ is the aspect ratio, and

$$D_{\mathrm{w}} = \frac{\widetilde{D}/\widetilde{H}^2}{\widetilde{k}_{\mathrm{a}}\widetilde{C}_{\mathrm{u}}} \tag{2.2}$$

is the ratio of the rate at which ligand molecules diffuse through the solution-well, as characterized by the quotient of the molecular diffusion coefficient $\widetilde{D}$ and the squared solution-well height $\widetilde{H}$, to the forward reaction rate. The subscript w indicates that this independent variable has been scaled with the well dimensions. It is seen in Table 2.1 that D_{w} may assume values from $O(10^{-2})$ to $O(10^2)$. In the former limit the rate of forward reaction far exceeds the rate at which ligand molecules diffuse through the solution-well, while in the latter forward reaction proceeds at a much slower rate than diffusion through the solution-well.

The bottom boundary condition associated with (2.1a)–(2.1d) must reflect the fact that while diffusive flux normal to the biochemical gate is used in forming bound ligand, there is no-flux through the region $(\overline{x}, \overline{y}) \in \{[0,1] \setminus [\overline{x}_{\min}, \overline{x}_{\max}]\} \times 0$. These two conditions are expressed compactly as

$$(\mathbf{n} \cdot \nabla C)|_{\overline{y}=0} = \mathrm{Da_w} \; \chi_{\mathrm{s}} \; [-(1 - B)C(\overline{x}, 0, t) + KB]. \tag{2.3}$$

In (2.3) $\mathbf{n} = (0, -1)$ denotes the outward unit normal vector, and χ_{s} is the characteristic function defined as

$$\chi_{\mathrm{s}}(\overline{x}) = \left\{ \begin{array}{ll} 1 & \overline{x} \in [\overline{x}_{\min}, \overline{x}_{\max}], \\ 0 & \overline{x} \notin [\overline{x}_{\min}, \overline{x}_{\max}]. \end{array} \right. \tag{2.4}$$

The parameter

$$K = \widetilde{k}_{\mathrm{d}}/(\widetilde{k}_{\mathrm{a}}\widetilde{C}_{\mathrm{u}}) \tag{2.5}$$

is the dimensionless equilibrium dissociation rate constant, given by the ratio of the dimensional dissociation rate constant $\widetilde{k}_{\mathrm{d}}$ to the forward reaction rate. Since the bound ligand concentration $B(x,t)$ is governed by the kinetics equation

$$\frac{\partial B}{\partial t} = (1 - B)C(\overline{x}, 0, t) - KB, \tag{2.6a}$$

$$B(\overline{x}, 0) = 0, \tag{2.6b}$$

the bottom boundary condition (2.3) can be expressed as

$$\frac{\partial C}{\partial y}(\overline{x}, 0, t) = \mathrm{Da_w} \, \chi_{\mathrm{s}} \, \frac{\partial B}{\partial t}. \tag{2.7}$$

Thus the complete partial differential equation system is given by (2.1), (2.6), and (2.7).

In equations (2.3) and (2.7), the important dimensionless parameter

$$\mathrm{Da_w} = \frac{\widetilde{k}_{\mathrm{a}}\widetilde{R}_{\mathrm{t}}}{\widetilde{D}/\widetilde{H}} \tag{2.8}$$

is the *Damköhler number*, defined as the ratio of the reaction velocity to the diffusion velocity. Note that both the numerator and denominator have dimensions of unit length per unit time. It is seen in Table 2.1 that $\mathrm{Da_w} \gg 1$, which implies that on these length scales the reaction velocity far exceeds the diffusion velocity. This is a direct consequence of the fact that there are multiple time and length scales associated with the experiment: ligand molecules must diffuse a distance on the order of millimeters to arrive at the biochemical gate, and the speed at which this transpires is far slower than the reaction velocity.

Using the fact that $\mathrm{Da_w} \gg 1$ reduces (2.7) to

$$\frac{\partial B}{\partial t} = 0, \tag{2.9}$$

which implies that, to leading order on these length scales, the processes of interest are in steady-state. To study reaction dynamics, we examine diffusion of ligand molecules in the vicinity of the biochemical gate by introducing the boundary layer coordinates

$$x = \frac{\overline{x} - 1/2}{l_s}, \qquad y = \frac{\epsilon}{l_s}\overline{y}. \tag{2.10}$$

In (2.10) the very small parameter

$$l_s = \frac{\widetilde{l}_{\mathrm{s}}}{\widetilde{L}} \tag{2.11}$$

is the ratio of biochemical gate length $\widetilde{l}_{\mathrm{s}}$ to the solution-well length $\widetilde{L}$. Introducing

these scalings into (2.1a)–(2.1d) and (2.7) yields

$$\frac{\partial C}{\partial t} = D \left(\frac{\partial^2 C}{\partial x^2} + \frac{\partial^2 C}{\partial y^2} \right), \tag{2.12a}$$

$$C(x, y, 0) = 0, \tag{2.12b}$$

$$C(x, \epsilon/l_\mathrm{s}, t) = 1, \tag{2.12c}$$

$$\frac{\partial C}{\partial x}(-1/(2l_\mathrm{s}), y, t) = \frac{\partial C}{\partial x}(1/(2l_\mathrm{s}), y, t) = 0, \tag{2.12d}$$

$$\frac{\partial C}{\partial y}(x, 0, t) = \mathrm{Da} \frac{\partial B}{\partial t} \chi_\mathrm{s}. \tag{2.12e}$$

The kinetics equation (2.6) becomes

$$\frac{\partial B}{\partial t} = (1 - B)C(x, 0, t) - KB, \tag{2.13a}$$

$$B(x, 0) = 0. \tag{2.13b}$$

Observe that transitioning to boundary layer coordinates has the effect of rescaling D_w and Da_w. The parameter

$$D = \frac{\widetilde{D}/\widetilde{l}_\mathrm{s}^2}{\widetilde{k}_\mathrm{a}\widetilde{C}_\mathrm{u}} \tag{2.14}$$

is the ratio of the diffusive time scale in the boundary layer $\widetilde{D}/\widetilde{l}_\mathrm{s}^2$ to the forward reaction rate, and since $D \gg 1$ the rate of diffusion within the boundary layer far exceeds the forward reaction rate. This is not surprising as we are considering picomolar to femtomolar ligand concentrations. Furthermore

$$\mathrm{Da} = \frac{\widetilde{k}_\mathrm{a}\widetilde{R}_\mathrm{t}}{\widetilde{D}/\widetilde{l}_\mathrm{s}} \tag{2.15}$$

is the Damköhler number associated with these length scales. Since Da is an $O(1)$ to $O(10)$ parameter, on these length scales the reaction velocity is the same as or only slightly faster than the diffusion velocity. Equation (2.12e) then implies that reaction balances diffusion within the boundary layer.

2.2. Integrodifferential Equation Reduction. Since $D \gg 1$, we neglect the left hand side of (2.12a) which reduces this equation to

$$\nabla^2 C = 0. \tag{2.16}$$

Physically, equation (2.16) implies that near the surface C is in a quasi-steady-state and change in the unbound concentration is driven by the surface-reaction (2.12e). Furthermore, since $l_\mathrm{s} \ll 1$ we are not concerned with satisfying the no-flux conditions (2.12d) and take our domain to be the infinite strip $\mathbb{R} \times [0, \epsilon/l_\mathrm{s}]$. This idealization is physically motivated and justified by the fact that the biochemical gate occupies a very narrow portion of the well surface, so the left and right boundaries of the solution-well will not appreciably affect ligand binding.

To solve the resulting set of PDEs we seek solutions of the form

$$C(x, y, t) = 1 + C_\mathrm{b}(x, y, t), \tag{2.17}$$

where C_b satisfies

$$\nabla^2 C_b = 0, \tag{2.18a}$$

$$C_b(x, \epsilon/l_s, t) = 0, \tag{2.18b}$$

$$\frac{\partial C_b}{\partial y}(x, 0, t) = \mathrm{Da}\frac{\partial B}{\partial t}\chi_s, \tag{2.18c}$$

for $(x, y) \in \mathbb{R} \times [0, \epsilon/l_s]$. To solve (2.18) we introduce a Fourier transform in x, defining the Fourier transform as

$$(\mathcal{F}u)(\omega) := \hat{u}(\omega) = \int_{-\infty}^{\infty} u(x)\mathrm{e}^{i\omega x}\ \mathrm{d}x, \tag{2.19a}$$

so that the inverse Fourier Transform is given by

$$(\mathcal{F}^{-1}\hat{u})(x) = u(x) = \frac{1}{2\pi}\int_{-\infty}^{\infty} \hat{u}(\omega)\mathrm{e}^{-i\omega x}\ \mathrm{d}x. \tag{2.19b}$$

Applying a Fourier transform to (2.18) and solving the resulting equations in the frequency domain gives

$$\widehat{C}_b(\omega, y, t) = -\frac{\mathrm{Da}\ \sinh((\epsilon l_s^{-1} - y)\omega)}{\omega \cosh(\epsilon l_s^{-1}\omega)}\ \frac{\partial \widehat{B}}{\partial t}(\omega, t) \star \left(\frac{\sin(\omega/2)}{\omega/2}\right), \tag{2.20}$$

where the convolution product $\star$ has been defined so that

$$\frac{\partial \widehat{B}}{\partial t}(\omega, t) \star \left(\frac{\sin(\omega/2)}{\omega/2}\right) = \int_{-\infty}^{\infty} \frac{\partial \widehat{B}}{\partial t}(\omega - \nu, t)\frac{\sin(\nu/2)}{\nu/2}\ \mathrm{d}\nu. \tag{2.21}$$

However, in order to study the dynamics of interest a closed-form of $C(x, y, t)$ on the surface $y = 0$ is required. This is aquired by applying the convolution theorem after calculating

$$f(x) = \frac{1}{2\pi}\int_{-\infty}^{\infty} \frac{\tanh(a\omega)}{\omega}\mathrm{e}^{-i\omega x}\ \mathrm{d}\omega. \tag{2.22}$$

Observe that when $x = 0$ the integrand decays at a rate of $1/\omega$ as $\omega \to \pm\infty$. Thus the integrand of (2.22) is not integrable when $x = 0$, and f is singular at the origin. The evaluation of (2.22) may then be separated into two cases: when $x > 0$ and when $x < 0$. We consider the latter by constructing a sequence of contours in the complex plane in the manner depicted in Figure 2.1. To fix notation we let $C^{(n)} = \sum C_j^{(n)}$.

The hyperbolic tangent function has countably infinite singularities along the imaginary axis, so the path of integration cannot intersect any of these singularities. The singularities will occur when $\omega = 0$ or

$$\omega = \frac{\pi i(2n + 1)}{2a}. \tag{2.23}$$

Note the contour depicted in Figure 2.1 does not pass through the singularity at the origin; in fact, since

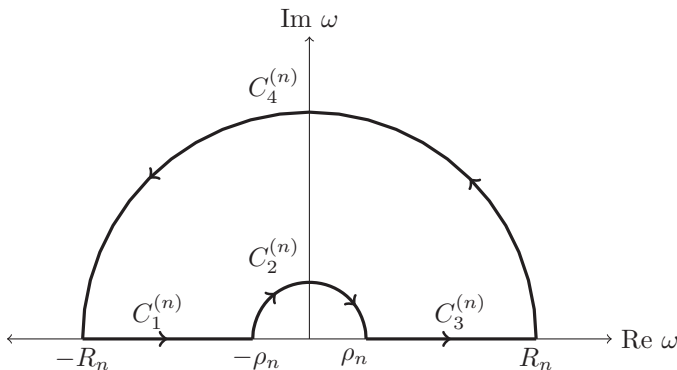$$\lim_{\omega \to 0} \tanh(a\omega) = 0 \tag{2.24}$$

FIG. 2.1: *The contour used to calculate (2.22) when $x < 0$.*

this singularity would not have contributed to (2.22) if we had placed the semi-circle of radius ρ_n in the lower half-plane. Thus taking the radii of our semi-circles to be

$$\rho_n = \pi/((n+2)a), \tag{2.25a}$$

$$R_n = \pi n/a, \tag{2.25b}$$

the path of integration will never intersect any of the singularities and Cauchy's Residue Theorem may be applied:

$$\oint_{C^{(n)}} \frac{\tanh(a\omega)}{\omega} \mathrm{e}^{-i\omega x} \, \mathrm{d}\omega = 2\pi i \sum_{k=0}^{n-1} I(C^{(n)}, a_k) \, \mathrm{Res}\left(\frac{\tanh(a\omega)}{\omega} \mathrm{e}^{-i\omega x}; \alpha_n\right). \tag{2.26}$$

Calculating residues and letting n approach infinity gives

$$\lim_{n \to \infty} \oint_{C^{(n)}} \frac{\tanh(a\omega)}{\omega} \mathrm{e}^{-i\omega x} \, \mathrm{d}\omega = 4 \sum_{k=0}^{\infty} \frac{\mathrm{e}^{(2k+1)\pi x/(2a)}}{(2k+1)}. \tag{2.27}$$

On the other hand,

$$\lim_{n \to \infty} \oint_{C^{(n)}} \frac{\tanh(a\omega)}{\omega} \mathrm{e}^{-i\omega x} \, \mathrm{d}\omega = \lim_{n \to \infty} \sum_{j=1}^{4} \oint_{C_j^{(n)}} \frac{\tanh(a\omega)}{\omega} \mathrm{e}^{-i\omega x} \, \mathrm{d}\omega. \tag{2.28}$$

One may show that the integral along $C_2^{(n)}$ vanishes as $n \to \infty$, and by using the fact that $x < 0$ it can also be shown that the integral along the far contour $C_4^{(n)}$ vanishes. From these facts and the Maclaurin series for $\tanh^{-1}(x)$ it follows that

$$f(x) = \frac{2}{\pi} \tanh^{-1}(\mathrm{e}^{\pi l_s x/(2\epsilon)}) \tag{2.29}$$

when $x < 0$. To evaluate (2.22) when $x > 0$ one may extend this integral to the complex plane by using the reflection of the contour depicted in Figure 2.1 about the real axis, shown in Figure 2.2, and use analogous arguments to show

$$f(x) = \frac{2}{\pi} \tanh^{-1}(\mathrm{e}^{-\pi l_s x/(2\epsilon)}) \tag{2.30}$$
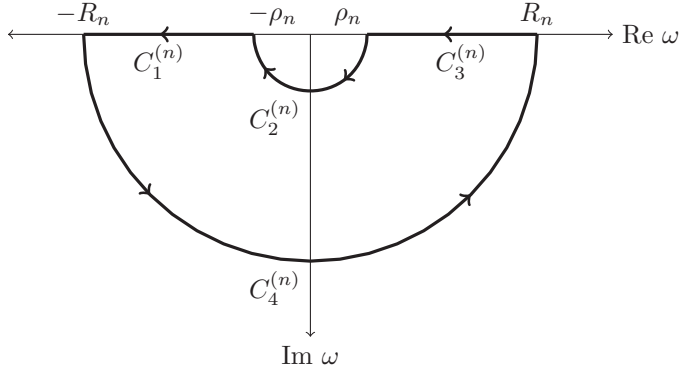
FIG. 2.2: *The contour used to calculate (2.22) when $x > 0$.*

when $x > 0$.

In summary the integral (2.22) is singular at the origin, given by (2.29) when $x < 0$, and (2.30) when $x > 0$. Putting these three observations together leads to the conclusion that

$$f(x) = \frac{2}{\pi} \tanh^{-1}(e^{-\pi l_s |x|/(2\epsilon)}) \tag{2.31}$$

almost everywhere on $[-1/2, 1/2]$. Thus applying the convolution theorem to (2.20) evaluated at $y = 0$ and substituting the resulting expression into (2.17) gives:

$$C(x, 0, t) = 1 - \frac{2 \, \text{Da}}{\pi} \int_{-1/2}^{1/2} \tanh^{-1}(e^{-\pi l_s |x-\nu|/(2\epsilon)}) \frac{\partial B}{\partial t}(\nu, t) \, d\nu. \tag{2.32}$$

Hence, the bound ligand concentration is governed by the IDE

$$\frac{\partial B}{\partial t} = (1 - B)\left(1 - \frac{2 \, \text{Da}}{\pi} \int_{-1/2}^{1/2} \tanh^{-1}(e^{-\pi l_s |x-\nu|/(2\epsilon)}) \frac{\partial B}{\partial t}(\nu, t) \, d\nu\right) - KB, \tag{2.33a}$$

$$B(x, 0) = 0. \tag{2.33b}$$

In (2.32) the term 1 represents the uniform injection concentration and the convolution integral represents depletion of unbound ligand at the surface due to reaction. As we shall see in Section 4 the non-local nature of the convolution (2.32) reflects the probabilistic nature of diffusion in the boundary layer near the surface, and the finite limits of integration encode the reflective boundary conditions to the left and right of the biochemical gate. However, we first turn our attention to finding a numerical approximation to the solution of (2.33).

3. Numerical Method.

3.1. Method of Lines Approximation. To discretize (2.33) we choose N equally-spaced discretization nodes x_i and partition $[-1/2, 1/2]$ into N distinct subintervals of length $\Delta x = 1/N$:

$$\left[-\frac{1}{2}, \frac{1}{2}\right] = \bigcup_{i=1}^{N} \left[x_i - \frac{\Delta x}{2}, x_i + \frac{\Delta x}{2}\right], \tag{3.1}$$

where $-1/2 = x_1 - \Delta x/2$ and $1/2 = x_N + \Delta x/2$. Then an approximation to (2.33) is found by applying the method of lines

$$B(x,t) \approx \sum_{i=1}^{N} h_i(t)\phi_i(x) \tag{3.2}$$

where the functions $h_i(t)$ are to be determined and subject to the initial condition $h_i(0) = 0$, and the functions $\phi_i(x)$ are locally defined piece-wise linear hat functions given by,

$$\phi_i(x) = \begin{cases} \dfrac{2}{\Delta x}[x - (x_i - \Delta x/2)] & \text{if } x \in [x_i - \Delta x/2, x_i), \\[2mm] \dfrac{2}{\Delta x}[(x_i + \Delta x/2) - x] & \text{if } x \in [x_i, x_i + \Delta x/2], \\[2mm] 0 & \text{else.} \end{cases} \tag{3.3}$$

Substituting (3.2) into (2.33a) and evaluating each side of the resulting equation at $x = x_j$ yields

$$h_j'(t) = (1 - h_j(t))\left(1 - \sum_{i=1}^{N} \frac{2 \, \text{Da} \, h_i'(t)}{\pi} \int_{-1/2}^{1/2} \tanh^{-1}(e^{-|x_j - \nu|\pi l_s/(2\epsilon)})\phi_i(\nu) \, d\nu\right)$$
$$- Kh_j(t), \tag{3.4}$$

for $j = 1, \ldots, N$. The solution of this nonlinear set of ODEs determines the time-dependent functions $h_j(t)$, however solving this system requires computing

$$\int_{-1/2}^{1/2} \tanh^{-1}(e^{-|x_j - \nu|\pi l_s/(2\epsilon)})\phi_i(\nu) \, d\nu. \tag{3.5}$$

Since $\tanh^{-1}(e^{-|x_j - \nu|\pi l_s/(2\epsilon)})$ exhibits logarithmic singularity at $\nu = x_j$, computing (3.5) using a quadrature rule requires great care, although (3.5) may be evaluated exactly. This is done by decomposing the basis functions (3.3) into their left and right parts:

$$\phi_{i,l}(x) = \begin{cases} \dfrac{2}{\Delta x}[x - (x_i - \Delta x/2)] & \text{if } x \in [x_i - \Delta x/2, x_i), \\[2mm] 0 & \text{else,} \end{cases} \tag{3.6}$$

and

$$\phi_{i,r}(x) = \begin{cases} \dfrac{2}{\Delta x}[(x_i + \Delta x/2) - x] & \text{if } x \in [x_i, x_i + \Delta x/2], \\[2mm] 0 & \text{else.} \end{cases} \tag{3.7}$$

Having decomposed the basis functions into their left and right parts (3.5) can be written as

$$\int_{-1/2}^{1/2} \tanh^{-1}(e^{-|x_j-\nu|\pi l_s/(2\epsilon)})\phi_i(\nu) \; d\nu$$

$$= \int_{-1/2}^{1/2} \tanh^{-1}(e^{-|x_j-\nu|\pi l_s/(2\epsilon)})\phi_{i,l}(\nu) \; d\nu \tag{3.8}$$

$$+ \int_{-1/2}^{1/2} \tanh^{-1}(e^{-|x_j-\nu|\pi l_s/(2\epsilon)})\phi_{i,r}(\nu) \; d\nu.$$

Since the two terms on the right hand side are related through a change of variables, it is sufficient to calculate

$$\int_{-1/2}^{1/2} \tanh^{-1}(e^{-|x_j-\nu|\pi l_s/(2\epsilon)})\phi_{i,l}(\nu) \; d\nu. \tag{3.9}$$

After changing variables, one may use the definition of $\tanh^{-1}(\cdot)$ and expand the integrand in terms of its Maclaurin series to find that it is a telescoping sum:

$$\int_{-1/2}^{1/2} \tanh^{-1}(e^{-|x_j-\nu|\pi l_s/(2\epsilon)})\phi_{i,l}(\nu) \; d\nu$$

$$= \sum_{n=0}^{\infty} \frac{2}{\Delta x} \int_0^{\Delta x/2} \frac{e^{-|w-x_j+x_i-\Delta x/2|(2n+1)\pi l_s/(2\epsilon)}}{2n+1} w \; dw. \tag{3.10}$$

In writing (3.10) we have formally exchanged the limit operations. Observe that the absolute value prevents one from integrating by parts directly; however, by using the fact that the discretization nodes are equally spaced one can show the computation may be partitioned in two distinct cases: when $x_j \geq x_i$ and $x_j < x_i$. Since the computation is analogous in each case we concern ourselves only with the former. Thus taking $x_j \geq x_i$ and integrating the right hand side of (3.10) by parts shows that (3.9) is equal to

$$\sum_{n=0}^{\infty} \left(\frac{2}{\Delta x}\right) \left(\frac{\Delta x \epsilon \; e^{-(x_j-x_i)(2n+1)\pi l_s/(2\epsilon)}}{(2n+1)^2 \pi l_s} - \frac{4\epsilon^2 \; e^{-(x_j-x_i)(2n+1)\pi l_s/(2\epsilon)}}{(2n+1)^3 \pi^2 l_s^2}\right.$$

$$\left. + \frac{4\epsilon^2 \; e^{-[\Delta x/2+(x_j-x_i)](2n+1)\pi l_s/(2\epsilon)}}{(2n+1)^3 \pi^2 l_s^2}\right). \tag{3.11}$$

To sum the series (3.11), we observe that one can use the definition of the polylogarithm of order s

$$\mathrm{Li}_s(z) = \sum_{k=1}^{\infty} \frac{z^k}{k^s} \tag{3.12}$$

to show

$$\sum_{n=0}^{\infty} \frac{z^{2n+1}}{(2n+1)^s} = \mathrm{Li}_s(z) - \frac{1}{2^s}\mathrm{Li}_s(z^2). \tag{3.13}$$

Hence when $x_j \geq x_i$

$$
\int_{-1/2}^{1/2} \tanh^{-1}(e^{-|x_j - \nu|\pi l_s/(2\epsilon)})\phi_{i,1}(\nu) \, d\nu
$$

$$
\begin{aligned}
= \left(\frac{2}{\Delta x}\right) & \left[\frac{\Delta x \epsilon}{\pi l_s} \left(\mathrm{Li}_2(e^{-(x_j - x_i)\pi l_s/(2\epsilon)}) - \mathrm{Li}_2(e^{-(x_j - x_i)\pi l_s/(\epsilon)})/4\right) \right. \\
& - \frac{4\epsilon^2}{\pi^2 l_s^2} \left(\mathrm{Li}_3(e^{-(x_j - x_i)\pi l_s/(2\epsilon)}) - \mathrm{Li}_3(e^{-(x_j - x_i)\pi l_s/(\epsilon)})/8\right) \\
& \left. + \frac{4\epsilon^2}{\pi^2 l_s^2} \left(\mathrm{Li}_3(e^{-[\Delta x/2 + (x_j - x_i)]\pi l_s/(2\epsilon)}) - \mathrm{Li}_3(e^{-[\Delta x/2 + (x_j - x_i)]\pi l_s/(\epsilon)})/8\right)\right].
\end{aligned}
\tag{3.14}
$$

The form of (3.14) when $x_j < x_i$ is similar. With a closed-form expression for the value for (3.8), the nonlinear set of ODEs (3.4) may be integrated with one's favorite linear multistage or multistep formula.

3.2. Convergence. Convergence of the previously described numerical method was measured by first computing a reference solution $B_{\mathrm{ref}}(x, t)$ from $t = 0$ to $t = 150$ with $N = 3^7 = 2187$ spatial basis functions. Then solutions $B_i(x, t)$ were computed with $N = 3^i$ basis functions and convergence was measured by calculating

$$
|| \, ||B_{\mathrm{ref}}(x, t) - B_i(x, t)||_{2, \, x}||_{\infty, \, t}
\tag{3.15}
$$

for $i = 1, \ldots, 6$. In (3.15) $|| \cdot ||_{2, \, x}$ denotes l_2 norm in x and $|| \cdot ||_{\infty, \, t}$ denotes the infinity norm in t. A logarithmic plot of these values is depicted in Figure 3.1. Despite the logarithmic singularity in (2.33a), the evidence in Figure 3.1 shows that our method of lines approximation to (2.33) enjoys excellent convergence on the order of $O(\Delta x^{1.0762})$.
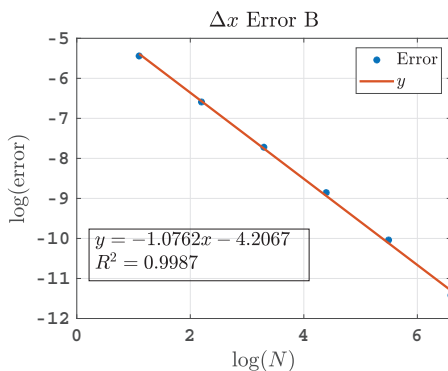

FIG. 3.1: *The values of (3.15) for $i = 1, \ldots, 6$ depicted together with the line $y = -1.0762x - 4.2067$, which was fit to the values of (3.15) with coefficient of determination of $R^2 = 0.9987$. Parameter values of $\mathrm{Da} = 66.42$, $K = 1$, $l_s = 10^{-3}$, and $\epsilon = 1$ were used.*

4. Results and Discussion. The results of our numerical simulations are depicted in Figure 4.1. Upon inspection one immediately notices the presence of a depletion region in the center of the biochemical gate for small t. As time progresses, the depletion regions narrows and becomes more shallow as the rate of bound ligand

production near the boundary decreases. The bound ligand concentration continues to become more spatially uniform until a chemical equilibrium is achieved, resulting in a balance between association and dissociation.
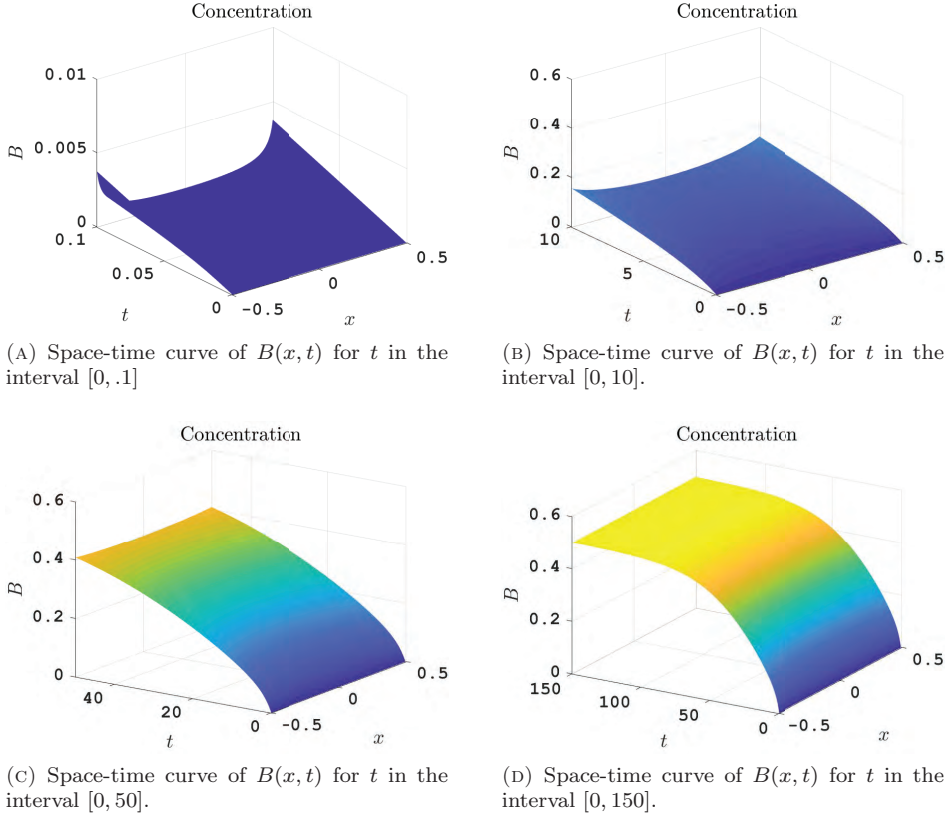

(A) Space-time curve of $B(x,t)$ for t in the interval $[0,.1]$

(B) Space-time curve of $B(x,t)$ for t in the interval $[0,10]$.

(C) Space-time curve of $B(x,t)$ for t in the interval $[0,50]$.

(D) Space-time curve of $B(x,t)$ for t in the interval $[0,150]$.

FIG. 4.1: *Method of lines approximation to the solution of (2.33) during different time intervals. Parameter values of* $\mathrm{Da} = 66.42$, $K = 1$, $l_\mathrm{s} = 10^{-3}$, *and* $\epsilon = 2/5$ *were used.*

Mathematically, the depletion region results from the singular convolution kernel

$$\tanh^{-1}(e^{-|(x-\nu)|\pi l_\mathrm{s}/(2\epsilon)}) \tag{4.1}$$

and the finite integration limits. In Figure 4.2 the convolution kernel has been depicted, centered at both $x = 0$ and $x = -1/2$. When the convolution kernel is centered at $x = 0$ it acts as a two-sided influence function. The singularity at $x = 0$ reflects the high likelihood that a ligand molecule directly above the origin will diffuse to the surface and bind with an available receptor site there; however, in the unstirred layer ligand molecules diffusing into the surface bind with neighboring receptor sites. Figure 4.2 reveals the likelihood of binding with a neighboring receptor site decays with the distance away from the source, although it is never zero since $\tanh^{-1}(e^{-|x-\nu|\pi l_\mathrm{s}}/(2\epsilon))$ is supported almost everywhere on the real line. Conversely, when the kernel is centered at $x = -1/2$ Figure 4.2 shows that it acts as a one-sided influence function. The finite limits of integration in (2.33a) imply that in this case the convolution kernel

influences the bound ligand concentration most at $\nu = -1/2$, and has a monotonically decreasing influence progressing from $\nu = -1/2$ to $\nu = 1/2$. Thus the finite limits of integration encode the reflective boundary conditions. To the right of $x = -1/2$ ligand molecules spread out and diffuse into the surface, while to the left they are merely reflected.
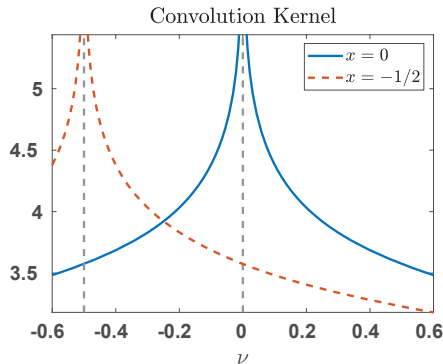

FIG. 4.2: *The convolution kernel* $\tanh^{-1}(e^{-|x-\nu|\pi l_s/(2\epsilon)})$ *centered at $x = 0$ (solid line), and at $x = -1/2$ (dashed line). Parameter values of $l_s = 10^{-3}$ and $\epsilon = 2/5$ were used.*

The average concentration across the biochemical gate

$$\overline{B}(t) = \int_{-1/2}^{1/2} B(x,t) \, \mathrm{d}x \tag{4.2}$$

is shown in Figure 4.3a for three values of $\widetilde{k}_a$. The average concentration (4.2) is proportional to the electrostatic potential applied to the biochemical gate, and thereby the electric current across the semiconducting channel, allowing direct comparison to measurements. Increasing the association rate constant results in a larger Damköhler number, reflecting the enhanced velocity of reaction relative to diffusion. From (2.33) it is clear that this results in wider and deeper depletion regions, which impede current flow near the boundaries of the biochemical gate before the rest of the semiconductor channel. This remarkable result is not directly observable experimentally, and provides physical insight into the origin of the measured signal. We also remark that the transient phase of the signal grows with the association rate constant, behavior directly following from the fact that while the Damköhler number is directly proportional to $\widetilde{k}_a$ the equilibrium dissociation rate constant is inversely proportional to this quantity.

In Figure 4.3b the average concentration (4.2) has been shown for three values of $\widetilde{C}_u$. One notices the existence of a linear regime for small time during which all three signals exhibit identical behavior, until they depart on different trajectories to chemical equilibrium. The small-time linear regime is expected because primarily association occurs during this window and the kinetic association constants are all identical. Indeed, mapping (2.33a) to dimensional time shows the first term on the right hand side of this equation that drives association is proportional to $\widetilde{k}_a\widetilde{C}_u$, so after a critical concentration of unbound ligand at the surface is achieved the three signals transition to different dynamic behavior. Different chemical equilibria are achieved

because the steady solution to (2.33) is

$$B_\infty = \frac{1}{1 + K},\qquad(4.3)$$

and the equilibrium dissociation rate constant K is inversely proportional to $\widetilde{C}_u$. This agrees with our physical intuition since increasing $\widetilde{C}_u$ results in more kinetic interactions at the surface, and in turn a higher bound ligand concentration.
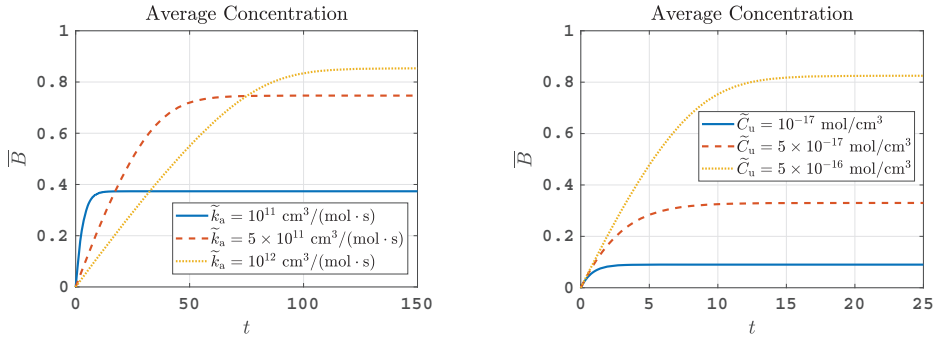
(A) The average concentration has been depicted for $\widetilde{k}_a = 10^{11}$, 5×10^{11}, and 10^{12} cm^3/(mol·s). This corresponded to Da = 6.64, 33.21, and 66.42; and $K = 1.67$, 0.33, and 0.17. In addition parameter values of $l_s = 10^{-3}$, and $\epsilon = 2/5$ were used.

(B) The average concentration has been depicted for $\widetilde{C}_u = 10^{-17}$, 5×10^{-17}, and 5×10^{-16} mol/cm^3. This corresponded to $K = 10$, 2, and 0.2. In addition parameter values of Da = 6.6420, $l_s = 10^{-3}$, and $\epsilon = 2/5$ were used.

Fig. 4.3: *The average concentration (4.2) for different values of $\widetilde{k}_a$ and $\widetilde{C}_u$.*

5. Conclusions. Accurate mathematical descriptions of Bio-FET experiments are required to enhance our qualitative and quantitative understanding of these instruments, making them more useful. These mathematical models form a basis for optimal design. The mathematical model developed herein takes the form of a diffusion equation, coupled to an equation describing reaction on the biochemical gate. Analysis of this set of nonlinear equations was complicated by the presence of multiple disparate time and length scales: ligand molecules diffuse a distance on the order of centimeters to arrive at the reacting surface, whose length scale is on the order of micrometers. Furthermore, kinetic interactions on the surface proceeded on a much faster time scale than diffusion through the solution-well. However, by employing the appropriate characteristic time and length scales our model reduces to a quasi-steady transport equation for the unbound ligand concentration C, coupled to an equation describing the evolution of the bound ligand concentration B. Employing the residue theorem allows the further reduction of this set of equations to a single nonlinear IDE in terms of the reacting species concentration. Despite the presence of a singular convolution kernel, this equation has been solved to first-order accuracy without the need to resort to specialized quadrature techniques to evaluate (3.5). Results of our numerical simulations reveal the presence of a depletion region in the center of the biochemical gate, which influences the measured signal by non-uniformly altering the surface-potential of the semiconductor channel.

In addition to providing insight into the origin of the measured signal, the present model provides a sound theoretical basis for parameter estimation and optimal design.

One could seek to maximize sensitivity by coupling the present model with one for carrier-transport, such as presented in [13]. In this case, the resulting coupled IDE-PDE system would undoubtedly require numerical treatment, most likely a nonlinear variational approach [11] and associated optimal control [12]. An analysis of how control and observability properties change as a function of the biochemical gate [29] is a future research direction the authors plan to pursue.

REFERENCES

[1] D. K. Armani, T. J. Kippenberg, S. M. Spillane, and K.J. Vahala, *Ultra-high-Q toroid microcavity on a chip*, Letters to Nature, 421 (2003), pp. 925.

[2] B. B. K., Y.-L. Zheng, V. Shukla, N. D. Amin, P. Grant, and H. C. Pant, *TFP5, a peptide derived from P35, a CDK5 neuronal activator, rescues cortical neurons from glucose toxicity*, Journal of Alzheimer's Disease, 39:4 (2014), pp. 899–909.

[3] S. Baumgartner, M. Vasicek, A. Bulyha, N. Tassotti, and C. Heitzinger, *Analysis of field-effect biosensors using self-consistent 3D drift-diffusion and Monte-Carlo simulations*, Procedia Engineering, 25 (2011), pp. 407–410.

[4] R. W. Boyd and J. E. Heebner, *Sensitive disk resonator photonic biosensor*, Applied Optics, 40:3 (2001), pp. 5742–5747.

[5] A. Cardone, H. Pant, and S. A. Hassan, *Specific and non-specific protein association in solution: computation of solvent effects and prediction of first-encounter modes for efficient configurational bias monte carlo simulations*, The Journal of Physical Chemistry B, 117:41 (2013), pp. 12360–12374.

[6] Y. Cui, Q. Wei, H. Park, and C. M. Lieber, *Nanowire nanosensors for highly sensitive and selective detection of biological and chemical species*, Science, 293 (2001), (5533) pp. 1289–1292.

[7] R. Dhavan and L.-H. Tsai, *A decade of CDK5*, Nature reviews. Molecular Cell Biology, 2:10 (2001), pp. 749.

[8] P. K. Drain, L. Gounder, F. Sahid, and M.-Y. Moosa, *Rapid urine LAM testing improves diagnosis of expectorated smear-negative pulmonary tuberculosis in an HIV-endemic region*, Scientific reports, 6 (2016), 19992.

[9] R. M. Evans, A. Balijepalli, and A. J. Kearsley, *Transport phenomena in biological field effect transistors*, 2019. Submitted.

[10] K. Fosgerau and T. Hoffmann, *Peptide therapeutics: current status and future directions*, Drug Discovery Today, 20:1 (2015), pp. 122–128.

[11] R. Glowinski, *Numerical Methods for Nonlinear Variational Problems*, Springer, New York, NY, 1984.

[12] R. Glowinski, J.-L. Lions, and J. He, *Exact and approximate controllability for distributed parameter systems: a numerical approach (Encyclopedia of Mathematics and its Applications)*, Cambridge University Press, 2008.

[13] C. Heitzinger, N. J. Mauser, and C. Ringhofer, *Multiscale modeling of planar and nanowire field-effect biosensors*, SIAM Journal on Applied Mathematics, 70:5 (2010), pp. 1634–1654.

[14] S. Henrich, O. M. H. Salo-Ahen, B. Huang, F. F. Rippmann, G. Cruciani, and R. C. Wade, *Computational approaches to identifying and characterizing protein binding sites for ligand design*, Journal of Molecular Recognition, 23:2 (2010), pp. 209–219.

[15] B. Ilic, H. G. Craighead, S. Krylov, W. Senaratne, C. Ober, and P. Neuzil, *Attogram detection using nanoelectromechanical oscillators*, Journal of Applied Physics, 95:7 (2004), pp. 3694–3703.

[16] D. Johannsmann and G. Brenner, *Frequency shifts of a quartz crystal microbalance calculated with the frequency-domain lattice–boltzmann method: application to coupled liquid mass*, Analytical chemistry, 87:14 (2015), pp. 7476–7484.

[17] W. Knoll, *Interfaces and thin films as seen by bound electromagnetic waves*, Annual Review of Physical Chemistry, 49:1 (1998), pp. 569–638.

[18] D. Landheer, G. Aers, W. R. McKinnon, M. J. Deen, and J. C. Ranuarez, *Model for the field effect from layers of biological macromolecules on the gates of metal-oxide-semiconductor transistors*, Journal of Applied Physics, 98:4 (2005), 044701.

[19] S. D. Lawn and A. Gupta-Wright, *Detection of lipoarabinomannan (LAM) in urine is indicative of disseminated tb with renal involvement in patients living with HIV and advanced immunodeficiency: evidence and implications*, Transactions of the Royal Society of Tropical Medicine and Hygiene, 110:3 (2016), pp. 180–185.

[20] P. Mohanty, Y. Chen, X. Wang, M. K. Hong, C. L. Rosenberg, D. T. Weaver, and S. Erramilli, *Field effect transistor nanosensor for breast cancer diagnostics*, arXiv:1401.1168 [q-bio.QM], 2014.

[21] A. K. Naik, M. S. Hanay, W. K. Hiebert, X. L. Feng, and M. L. Roukes, *Towards single-molecule nanomechanical mass spectrometry*, Nature Nanotechnology, 4:7 (2009), pp. 445–450.

[22] F. Pouthas, C. Gentil, D. Côte, and U. Bockelmann, *DNA detection on transistor arrays following mutation-specific enzymatic amplification*, Applied Physics Letters, 84:9 (2004), pp. 1594–1596.

[23] M. Rodahl, F. Höök, A. Krozer, P. Brzezinski, and B. Kasemo, *Quartz crystal microbalance setup for frequency and Q-factor measurements in gaseous and liquid environments*, Review of Scientific Instruments, 66:7 (1995), pp. 3924–3930.

[24] J. Su, *Label-free single exosome detection using frequency-locked microtoroid optical resonators*, ACS Photonics, 2:9 (2015), pp. 1241–1245.

[25] G. Tulzer, S. Baumgartner, E. Brunet, G. C. Mutinati, S. Steinhauer, A. Köck, P. E. Barbano, and C. Heitzinger, *Kinetic parameter estimation and fluctuation analysis of CO at SnO_2 single nanowires*, Nanotechnology, 24:31 (2013), 315501.

[26] G. Walsh, *Biopharmaceutical benchmarks 2014*, Nature Biotechnology, 32:10 (2014), pp. 992–1000.

[27] S. Wang, X. Shan, U. Patel, X. Huang, J. Lu, J. Li, and N. Tao, *Label-free imaging, detection, and mass measurement of single viruses by surface plasmon resonance*, Proceedings of the National Academy of Sciences, 107:37 (2010), pp. 16028–16032.

[28] W. U. Wang, C. Chen, K.-h. Lin, Y. Fang, and C. M. Lieber, *Label-free detection of small-molecule–protein interactions by using nanowire nanosensors*, Proceedings of the National Academy of Sciences of the United States of America, 102:9 (2005), pp. 3208–3212.

[29] E. Zuazua, *Controllability and observability of partial differential equations: some results and open problems*, in "Handbook of differential equations: evolutionary equations", volume 3, pp. 527–621. Elsevier, 2007.